J. Fluid Mech. (1998), *vol.* 375, *pp.* 179–202. Printed in the United Kingdom

Natural convection in a horizontal concentric cylindrical annulus: oscillatory flow and transition to chaos

By G. LABONIA[1] AND G. GUJ[2]†

[1] Università di Roma *La Sapienza*, Dipartimento di Meccanica e Aeronautica, Via Eudossiana 18, 00184 Roma, Italy

[2] Università di Roma Tre, Dipartimento di Ingegneria Meccanica e Industriale, Via della Vasca Navale 79, 00146 Roma, Italy

(Received 8 January 1997 and in revised form 22 June 1998)

An experimental study of transition from steady laminar to chaotic flow in a horizontal annulus between concentric cylinders is conducted for $0.90\times10^5 \leqslant Ra_L \leqslant 3.37\times10^5$. Qualitative information on the averaged thermal field is obtained by an interferometric method, whereas the kinematics are visualized by using smoke lines. The transition from steady to unsteady mono- and multi-periodic regimes is accurately studied by a CTA and CCA combined hot-wire technique. Different data analyses are performed in order to differentiate the forms of transition.

1. Introduction

The study of flow and heat transfer in natural convection in horizontal cylindrical annuli has received some attention in the past years. This was due mainly to two different aspects: the engineering applications such as gas-insulated electric transmission cables and theoretical interest since the chaotic transition phenomena are not completely understood.

Gas-insulated electric cables consist of a spaced cylindrical conductor heated by the Joule effect and a coaxial sheath with a gap of the order of magnitude of the inner diameter. These gas-insulated cables are quite important in both underground power transmission and high-voltage substations. In underground power transmission cables electrical insulation is obtained using air and the order of magnitude of geometrical dimensions and temperature gaps is such that the Rayleigh number is in the range $10^4 \sim 10^5$. In high-voltage substations, the use of SF_6 as an insulator is becoming very attractive due to the possibility of reducing the space and cost requirements because of the excellent dielectric strength and high arc-extinguishing characteristics. For these applications the Rayleigh number (Ra_L) is in the range $10^5 \sim 10^6$.

The phenomenon of transition to chaos in a horizontal cylindrical annulus is also very attractive from a theoretical point of view as it presents a very good repeatability in the different stages of transition. This behaviour is due to the strong and well defined basic flow in the steady-state condition. As a matter of fact the structures of this flow depend neither on the initial conditions nor on the transient of the system, in contrast with Rayleigh–Bénard systems (Bergé, Pomeau & Vidal 1984).

† Author to whom correspondence should be addressed.

This well defined behaviour permits a close study of chaotic transition phenomena, with the goal of experimentally validating the scenarios of transition to chaos.

Many experimental investigations as well as numerical simulations have been conducted for studying natural convection in horizontal cylindrical annuli in steady conditions. In particular Kuehn & Goldstein (1976) presented an experimental and theoretical study of this problem together with a complete review of the relevant, now dated, literature; Kuehn & Goldstein (1978) experimentally studied the case of vertical eccentric cylinders. Chakrabarti, Probert & Shilton (1983) analysed by an interferometric technique the system with a cold inner cylinder. Guj, Iannetta & Moretti (1992) used the same technique for evaluating the thermal field and heat transfer in a horizontal eccentric cylindrical annulus. Also, the numerical studies are restricted to the case of steady flow conditions in concentric and eccentric annuli (Kuehn & Goldstein 1976; Cho, Chang & Park 1982; Wang & Bau 1988; Guj & Stella 1995). The study of unsteady conditions has received less attention due to difficulties connected with the possible mechanisms that can appear in the transition from steady to turbulent conditions by changing the independent dimensionless parameters, which are: Rayleigh number (Ra) (or Grashof number, Gr), Prandtl number (Pr) and dimensionless gap ℓ. As clearly described in the paper of Bishop, Carley & Powe (1968) and Prusa & Yao (1983) two different oscillatory flow patterns can appear: the first is basically a two-dimensional tangential instability in the form of two eddies, while the second is of the three-dimensional type. Furthermore multicellular situations in the upper part of the annulus can appear for very low ℓ (Prusa & Yao 1983) and cross roll configurations can be present due to the end wall. Bishop *et al.* (1968) also gave the correlation equations in terms of oscillating flow parameters (amplitude, period and wavelength) for a wide range of Gr and ℓ. They presented an exponential reduction of periodicity for increasing Gr with an exponent of 0.44 and this behaviour is qualitatively confirmed by the experimental work of Miki *et al.* (1988) and by the numerical simulation of Ohya *et al.* (1988). So, to our knowledge, no quantitative systematic studies are available in the literature which focus their attention on the mechanism of transition from steady state to chaotic behaviour in its initial stage.

Thus, in the present paper, the transition from steady to unsteady chaotic flow conditions in a horizontal annulus between concentric cylinders is experimentally studied because this dynamical behaviour may happen in the Ra range of real electrical applications. The combination of a dual sensor probe technique of the hot/cold type for very accurate simultaneous local velocity and temperature measurements (Guj, Labonia & Stella 1997), an interferometric method for averaged thermal field evaluation (Guj *et al.* 1992) and a kinematical flow visualization permit the mechanism of transition to chaos to be determined in a systematic way for the given geometry of the annulus. The Ra_L is varied in the range 0.90×10^5 and 3.37×10^5 which correspond to steady state and chaotic conditions, respectively.

A wide data analysis is performed on very long time histories (order of $4\,h$) and a large number of samples (order of 6×10^5). Different indicators such as power spectral density (PSD), phase trajectories (PT), Poincaré section (PS), fractal dimension (FD), Lyapunov exponents (LE) and probability density functions (PDF) are adopted to define uniquely the dynamical behaviour of the system while kinematical and thermal visualization have given qualitative information on flow structures and oscillatory modes.

According to Bishop *et al.* (1968) and Miki *et al.* (1988) these indicators all seem to confirm that the first transition from steady to unsteady behaviour happens in a three-dimensional manner at $Ra_L \simeq 1.82 \times 10^5$ with a monoperiodic mode at very low

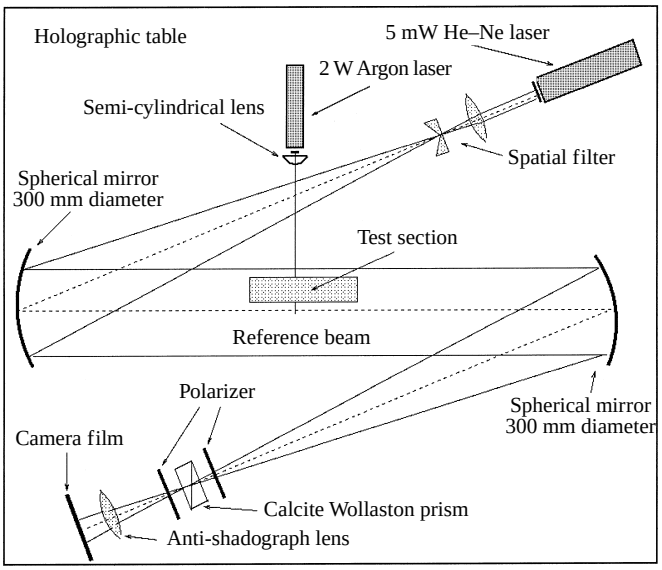

FIGURE 1. Sketch of the experimental setup (interferometer and flow visualization).

frequency. For $Ra_L = 2.13 \times 10^5$ a second incommensurable frequency appears and it seems to take energy from the lower frequency, which tends to disappear. In the final stage of the transition to chaos two new modes appear with incommensurable frequencies. We argue that the mechanism of the transition to chaos follows the Curry–Yorke scenario (Bergé *et al.* 1984), the energy of the intermediate frequency mode being two orders of magnitude less than that of the other two. The PSDs do not show any inertial range and the power laws that can be found for some Ra_L present scaling exponents which seem to refer to a dissipative range.

2. Experimental setup

The test section, the optical elements, which are used for interferometry and flow visualizations, and the dual sensor probes are mounted on a holographic table to reduce the high-frequency vibration noise from the floor of the laboratory (figure 1).

2.1. *Test section*

The test section, which consists of a very long annulus (length $b = 362$ mm) filled with air at atmospheric pressure (a sketch of the geometry is shown in figure 2), was designed to present a large aspect ratio and to satisfy the interferometer accuracy requirements, that is the number of fringes, when using a two-beam interferometer within the considered temperature range.

The assembled apparatus is composed of two copper cylinders. The inner cylinder (diameter $d_i = 39.8$ mm) is heated by passing an alternating current through a resistor (50 Ω) and supported by two insulated bakelite supports. The outer cylinder (diameter $d_o = 94$ mm) has been built of two different sections separated by a 10 mm long copper ring, which contains the holes for inserting the probes. Water at isothermal conditions passes through two counter-rotating channels of a double helix. The isothermal conditions on the cylinder surfaces are checked by a system of fourteen Cr-Al thermocouples, which are positioned within 1 mm of the outer

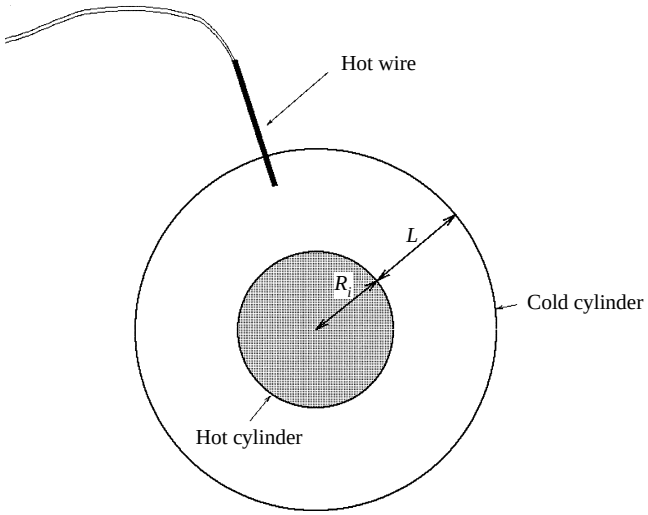

FIGURE 2. Sketch of the geometry of the test section and probe position.

surface of the cylinders. Six thermocouples have been positioned in the inner cylinder, whereas eight thermocouples have been positioned in the external one.

2.2. *Interferometer optical configuration*

According to the general theory of two-beam interferometry (Merzkirch 1974), we chose the interferometer setup to have a parallel beam of light passing through the test field. The interferometer used (sketched in figure 1), based on the interferometrical methodology proposed by Carlomagno (1986), is described in detail in (Guj *et al.* 1992) and combines the advantages of RBI (reference beam interferometry) of Mach–Zehnder type with the setup simplicity of SI (shearing interferometry).

2.3. *Hot-wire anemometer techniques*

Simultaneous measurements of velocity and temperature by a dual sensor probe in unsteady natural convection flows with large temperature gaps (order of 50 °C or more) are particularly complex due to two main reasons; namely (i) the nonlinear relationship between output voltage from the sensors and temperature, (ii) contamination of the CCA voltage by the velocity. Therefore a special hot/cold dual sensor probe technique of wire type has been studied and installed for performing such measurements. Details of the calibration and measurement procedure and the numerical technique to process the signals are reported in Guj *et al.* (1997). Therefore only a summary is given here.

Instrumentation. The velocity and temperature measurements have been performed using a dual sensor probe DISA 55P71 with two parallel sensors of 5 μm diameter about 1 mm long and an AN 1003 Lab-System hot-wire system. One sensor was connected to a constant temperature module (CTA), while the other was connected to a constant current module (CCA).

Directional sensitivity. In an experimental study Guj *et al.* (1997) have verified that, in agreement with the theory, the directional sensitivity of the hot wire vanishes for $\|\boldsymbol{v}\| \to 0$ (Brunn 1995). Then, in the present range of velocity ($\|\boldsymbol{v}\|_{max} \simeq 0.15\mathrm{m\,s^{-1}}$), the hot wire is sensitive directly to the velocity modulus ($v = \|\boldsymbol{v}\|$), all sensitivity coefficients being equal to about 1.

Calibration procedure. A specially designed low-velocity calibrator has been designed and used for vertical velocity up to $0.2\,\mathrm{m\,s^{-1}}$. This calibrator accounts for the effect of natural convection self-induced by the hot wire and allows the temperature of the air flow to be changed in a wide range. The two calibration surfaces

$$e_{CCA} = e_{CCA}(v,\ T), \quad e_{CTA} = e_{CTA}(v,\ T) \tag{1}$$

are obtained by performing velocity calibration curves at several (seven in the present case) constant temperatures. The temperature is measured by a system of Cr-Al thermocouples.

Data acquisition. A constant offset has been given to both CCA and CTA signals to reduce the mean value, then both are amplified by the respective modules from 6 to 35 times. The amplified signals are then filtered with a cut off frequency of 25 Hz by means of an analogic filter Keemo VBF8 (roll off of 48 dB/octave) and amplified from 10 to 100 times in order to reach the full scale of the A/D converter (12 bit) and to obtain the maximum resolution. The acquisition is performed by DATS Acquire System (Prosig Consultant Ltd) on a PC 486 with a sampling rate of 1024 Hz.

Measurement procedure and data processing. In each experiment the apparatus is left at constant conditions for at least 3 hours to reach a steady state or fully developed condition. This condition is then checked for the following ten minutes by local velocity measurements or by visual analysis of the interferometric fringes. Then, ten decorrelated acquisitions of 1.050 Ksamples per channel are performed in about 4 hours, with a sampling rate of 1024 Hz. The offset is added to the deamplified digital signal and a digital low pass filter is applied before resampling the signal to 64 Hz. The simultaneously measured velocity and temperature are calculated by solving the nonlinear system of equations (1) using Newton's method. So, for each acquisition, the time histories for the quantities v and T are obtained for 1024 s (65536 samples).

System accuracy. The accuracy in the evaluation of velocity and temperature at the measurement point has been evaluated by reprocessing a large number of calibration points by means of the procedure described above. The uncertainty in velocity is $0.6 \times 10^{-3}\,\mathrm{m\,s^{-1}}$, that in temperature is $0.2 \times 10^{-1}\ ^{\circ}\mathrm{C}$ for $0.02 < v < 0.2\ \mathrm{m\,s^{-1}}$ and $10 < T < 80\ ^{\circ}\mathrm{C}$ (Guj *et al.* 1997).

The effect of background noise has been evaluated by performing a measurement at two conditions: at rest ($\Delta T = 0\ ^{\circ}\mathrm{C}$) and steady ($\Delta T = 39\ ^{\circ}\mathrm{C}$). The PSD shows the expected isoenergetic power law with a slope of -1. It is worth noting that, due to the large amplification used (from 60 to 3500) the accuracy in the fluctuating component of velocity and temperature signals is orders of magnitude greater than that achieved for the mean components.

3. Physical model

A dimensional analysis of the problem is performed using the following variables: gap between the cylinders L, diameter of the inner cylinder d_i, temperature difference between the cylinders ΔT, thermal expansion coefficient β ($= 1/T$, T in K), modulus of gravitational acceleration g, thermal diffusivity α, kinematic viscosity ν and the cylinder longitudinal length b. This analysis leads to the following five independent dimensionless groups:

$$Ra_L = \frac{g\,\beta\,L^3\,\Delta T}{\nu\alpha}, \quad Pr = \frac{\nu}{\alpha}, \quad N_E = \beta\,\Delta T, \quad \ell = \frac{L}{d_i}, \quad \lambda = \frac{b}{d_i},$$

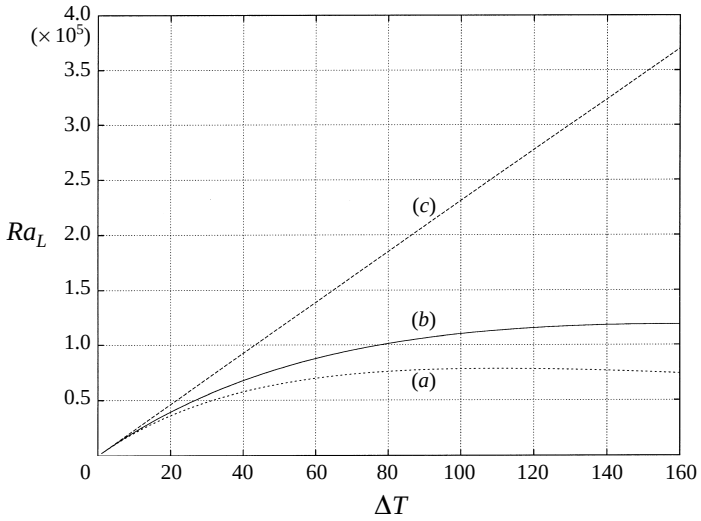

FIGURE 3. The Rayleigh number as a function of ΔT, to use as reference temperature for the fluid properties calculation: (*a*) T_i, (*b*) T_m, (*c*) T_o.

where Ra_L is the Rayleigh number, Pr is the Prandtl number, N_E is the expansion number, ℓ is the non-dimensional gap and λ is the aspect ratio. The effect of the expansion number is normally not considered to be significant, and it is usually neglected. In particular Bishop *et al.* (1968) demonstrated that the effects of N_E do not affect the value of the critical Grashof number (Gr_{crit}) and the frequency of the oscillating flow ($\tilde{f}$) which are the quantities under investigation in this paper. Therefore N_E is not included in our analysis.

The effect of variations of β, ν and α with time is not included in the dynamical analysis, due to the negligible value of both their sensitivity with respect to temperature and the small temperature fluctuation with time (table 1, § 5) during the dynamical behaviour.

Owing to the large variation of temperature in the annulus, the properties of the fluid (ν, α, β) are not considered constant in space at the different Ra_L conditions and the temperature for the fluid properties calculation is important in the evaluation of Ra_L. The three curves reported in figure 3 show Ra_L as a function of ΔT by using as a reference temperature (*a*) T_i, (*b*) $T_m = (T_i + T_o)/2$, (*c*) T_o where T_i (T_o) is the temperature of the inner (outer) cylinder; it is evident that the three curves superimpose for $\Delta T < 10$ °C, while for large ΔT the curve (*b*) is not a function of ΔT whereas the curve (*a*) decreases when ΔT increases. For this reason T_o has been chosen as a reference temperature instead of T_m usually used by other authors in smaller ΔT applications.

As reported by Bishop *et al.* (1968), edge effects might cause the numerical values of wavelength, $\tilde{f}$, Gr_{crit} and amplitude to vary somewhat as λ is reduced much below 9. Thus, since $\lambda = 13.4$, it is most unlikely that the oscillating flow condition detected is affected by the edge effects.

In our experiment $\ell = 0.68$, and Pr is nearly constant ($\simeq 0.71$) in the range of temperature considered.

It follows that Ra_L with the fluid properties defined with T_o can be considered the only independent control parameter for the dynamical system.

4. Dynamical characterization techniques

Many indicators are adopted to analyze and categorize the different dynamical behaviours of the system. In particular the following techniques have been used: power spectral density (PSD), phase trajectories (PT), Poincaré sections (PS), fractal dimension (FD), Lyapunov exponents (LE) and probability density functions (PDF).

4.1. *Power spectral density*

A standard PSD analysis has been performed on both velocity and temperature time series. A frequency resolution of $\Delta f = 0.97656 \times 10^{-3}$ Hz has been adopted in order to resolve the smallest physical frequency, and the PSD is evaluated from the ensemble averages of 10 decorrelated acquisitions.

4.2. *Phase trajectories and Poincaré sections*

The phase space is the mathematical space $\mathscr{R}^n$ in which each orthogonal coordinate represents a degree of freedom of the dynamical system. Usually the number of degrees of freedom is not known *a priori* and it is necessary to reconstruct both the phase space and the topology of the attractor by using a time delay technique (Takens 1981; Bergé *et al.* 1984) from the values of the variable $x(t)$ at the instant t and at $n-1$ other decorrelated instants. Then a phase pseudo-space is defined as

$$\boldsymbol{X}(t) = \{x(t),\ x(t+\tau), \ldots,\ x(t+(n-1)\tau)\}.$$

According to Bergé *et al.* (1984), the time delay (τ) is given by the first zero of the autocorrelation function. Different choices for τ have been tested for validation purposes in the range $0.8\,\tau \sim 3\,\tau$. The results are similar to the ones calculated with the criteria defined above.

In the following, we will call the trajectories in the phase pseudo-space PT. Analogously the PS consists of sectioning the trajectories and looking at these sections through a plane in a phase pseudo-space. In an $\mathscr{R}^3$ phase pseudo-space ($\{x(t),\ x(t+\tau),\ x(t+2\,\tau)\}$) we have adopted as PS the intersections between the trajectories and the plane $x(t) = x(t+\tau)$ looking at these sections along the (0, 1, 0) axis which gives the curves $\{[x(t),\ x(t+2\tau)]$ at $x(t) = x(t+\tau)\}$.

4.3. *Correlation (fractal) dimension*

There are many ways to define the dimension, $d(A)$, of a set A. The *correlation* dimension d_c (Grassberger & Procaccia 1983) has been adopted in the present work to estimate $d(A)$ due to the fact that for experimental data or high-dimensional dynamical systems d_c is very efficient to compute (Baker & Gollub 1990). The correlation dimension may be computed from the integral correlation function $C(r)$ equal to

$$C(r) = \lim_{N\to\infty} \frac{1}{N} \sum_{i=1}^{N} C_i(r), \tag{2}$$

N being the number of samples and

$$C_i(r) = \frac{1}{N-1} \times [\text{number of pairs i, j whose distance } \|\boldsymbol{x}_i - \boldsymbol{x}_j\| < r].$$

In our case we are working with two variables (v, T), and so we must define a distance $d(t)$ in the space (v, T) by non-dimensionalization of v and T as

$$d(t) = \|\boldsymbol{x}_i - \boldsymbol{x}_j\| = \left[\left(\frac{v_i - v_{med}}{\Delta v} - \frac{v_j - v_{med}}{\Delta v}\right)^2 + \left(\frac{T_i - T_{med}}{\Delta T} - \frac{T_j - T_{med}}{\Delta T}\right)^2\right] \quad (3)$$

with $\Delta v = v_{max} - v_{min}$ and $\Delta T = T_{max} - T_{min}$. Such a distance can be extended to the (v, T)^n space by using a time delay technique.

From the physical point of view, $C(r)$ is proportional to the average number of points that are inside the hypersphere with radius r centred on the generic point. For an attractor the fractal structure becomes a power law

$$C(r) \sim r^{d_c} \quad \text{for} \quad r \to 0. \quad (4)$$

The validity of this power law is limited to values of r reasonably small compared to the expansion of the attractor in the pseudo-space; as r increases, $C(r)$ saturates as r attains values comparable to the attractor size. On the other hand, the statistics fluctuations become negligible when $C(r) \times N^2$ is of the order of 100 (Atten & Malraison 1988).

4.4. *Lyapunov exponents*

For a nonlinear application $\boldsymbol{x}_{n+1} = f(\boldsymbol{x}_n)$, the Jacobian matrix $(J_{ij})_{\boldsymbol{x}_n}$ is equal to the matrix with the partial derivatives $((\partial f_i/\partial x_j)_{\boldsymbol{x}_n})$ as elements. The Lyapunov exponents are a sort of mean of the eigenvalues of $\boldsymbol{J}_{\boldsymbol{x}_n}$. By introducing the matrix $\boldsymbol{T}^n = \boldsymbol{J}_{\boldsymbol{x}_n}\boldsymbol{J}_{\boldsymbol{x}_{n-1}}\cdots\boldsymbol{J}_{\boldsymbol{x}_o}$ it is possible to show (Oseledec 1968) that, under ergodic requirements, the limit matrix

$$\Lambda_{\boldsymbol{x}} = \lim_{n\to\infty} \|\boldsymbol{T}^n\|^{1/n} \quad (5)$$

exists and does not depend to $\boldsymbol{x}_n$. The Lyapunov exponents are defined as the logarithm of the eigenvalues of $\Lambda_{\boldsymbol{x}}$.

We have evaluated the exponent with the largest real part using the method proposed by Benettin, Galgani & Strelcyn (1976). So we follow the evolution in time of a point $\boldsymbol{x}_i$ of the trajectory and a nearby point $\boldsymbol{x}_j$ belonging to a different portion of the trajectory. If $d(t)$ is the distance between $\boldsymbol{x}_i$ and $\boldsymbol{x}_j$ at the instant t the Lyapunov exponent is given by

$$\lambda = \lim_{t\to\infty} \log\left[\frac{d(t)}{d(t_o)}\right]. \quad (6)$$

The distance $d(t)$ is computed by equation (3).

4.5. *Probability density functions*

A standard PDF has been calculated for both the velocity and temperature time series. A Δv (ΔT) resolution equal to two times the v (T) accuracy has been adopted in order to reduce the statistical fluctuations, and the PDF is evaluated using 655 K samples.

5. Results and discussion

The temperature gap has been increased from 39 °C to 146 °C, that is Ra_L is varied from 0.90×10^5 to 3.37×10^5 for the considered radius ratio ($d_o/d_i = 2.36$). In this range of Ra_L several dynamical behaviours appear from steady state to chaotic

ΔT (°C)	$Ra_L \times 10^{-5}$	$\sigma_v \times 10^2$ (m s^{-1})	$\sigma_T \times 10$ (°C)	A_u	A_T	Dynamical state
39	0.90	0.043	0.070	1	1	Steady state
72	1.66	0.056	0.141	1.3	2.0	Steady state
79	1.82	1.353	5.147	26.4	36.3	Periodic regime
92	2.13	0.438	2.877	8.6	17.4	Quasi-periodic regime
102	2.36	0.600	4.877	11.1	26.6	Periodic regime
123	2.84	0.343	3.000	4.1	13.6	Quasi-periodic regime
146	3.37	0.723	10.956	5.6	41.8	Chaotic regime

TABLE 1. Statistics of the critical flow conditions.

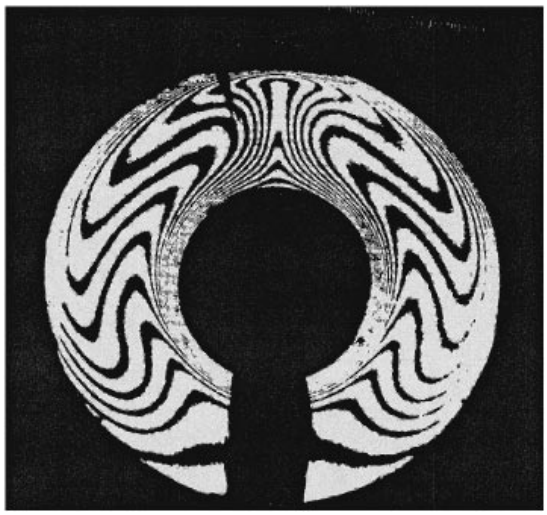

FIGURE 4. Interferometric thermal field for $Ra_L = 0.90 \times 10^5$. Note the position of the probe with respect to the plume.

conditions. According to Kuehn & Goldstein (1976) a steady structure is found for $Ra_L < 1.82 \times 10^5$. For this value of Ra_L the flow becomes oscillatory with only one, very low, frequency. The final transition mechanism to the chaotic condition is that of the Curry–Yorke model (Bergé *et al.* 1984): the chaos appears directly from a quasi-periodic regime with two frequencies, while in the intermediate range of Ra_L a transition of energy from low to high frequency has been detected. A large number of intermediate Ra_L values have been tested. All the conducted experiments are in agreement with the scenario presented in this paper.

A summary of the critical flow conditions which correspond to the transitional dynamical state of the system is reported in table 1 together with some statistical quantities. The turbulence level (σ_v) and temperature standard deviation (σ_T) give a global indication of the dynamical condition of the system, while $A_v = (\sigma_v/v)\,(v^{39}/\sigma_v^{39})$ and $A_T = (\sigma_T/\Delta T)\,(39/\sigma_T^{39})$ give a relative measure of the ratio between mean and fluctuating quantities with respect to steady-state conditions.

5.1. *Steady state*

At Ra_L up to 1.66×10^5 ($\Delta T = 72$ °C) the integral indicators (table 1) confirm that the flow is steady having $A_v = 1.3$ and $A_T = 2.0$, of the order of one. The thermal

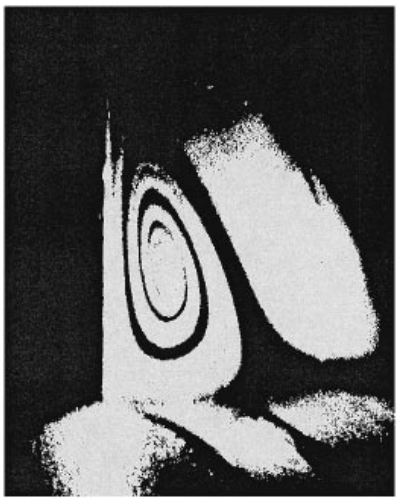

FIGURE 5. Kinematical flow visualization for $Ra_L = 0.90 \times 10^5$ ($\Delta T = 39$ °C) of the endwall effect (perspective view).

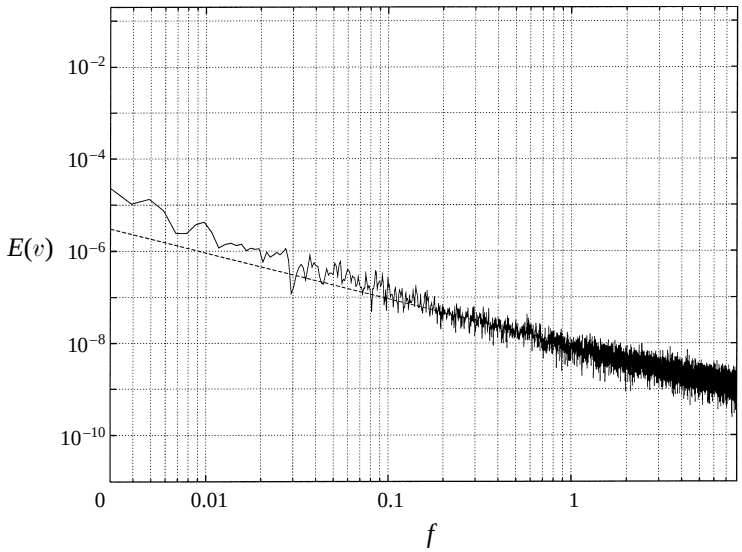

FIGURE 6. Power spectral density for $Ra_L = 0.90 \times 10^5$. Velocity.

field ($Ra_L = 0.90 \times 10^5$) obtained by the interferometric technique is shown in figure 4. The effect of the two recirculating cells is clearly shown as reported in Guj *et al.* (1992). Flow visualization along the axis of the annulus shows only the endwall effect (figure 5).

The slope of the PSD for these cases is equal to that of $Ra_L = 0$ (figure 6), due to the background noise. The linear fit for $Ra_L = 0.90 \times 10^5$ ($\Delta T = 39$ °C) is shown in all the PSDs at different Ra_L presented in the following, to give quantitative information on the signal to noise ratio in the Fourier space.

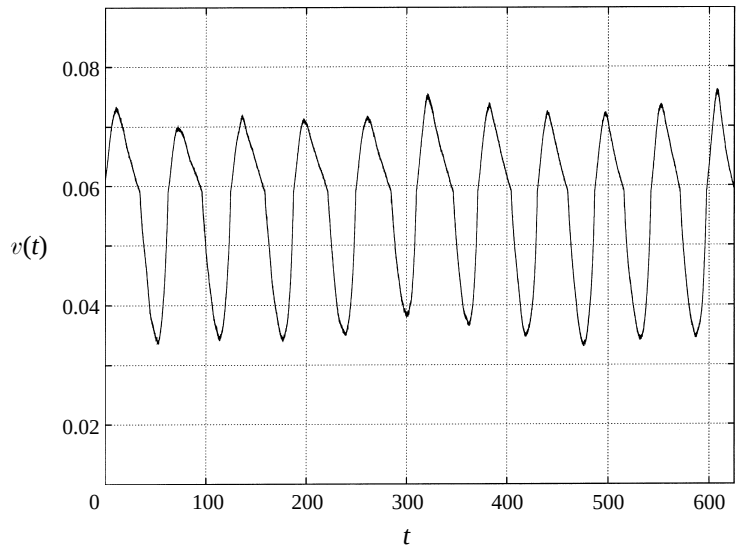

FIGURE 7. The velocity time history for $Ra_L = 1.82 \times 10^5$.

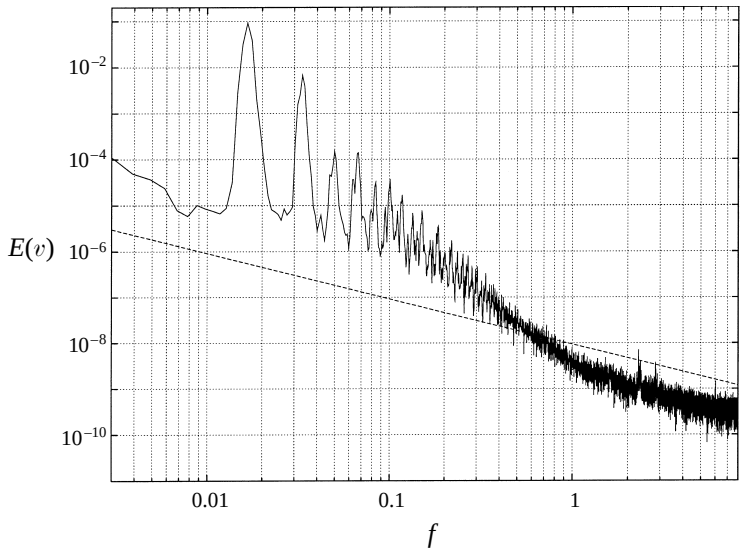

FIGURE 8. Power spectral density for $Ra_L = 1.82 \times 10^5$. Velocity.

5.2. *First periodic regime*

A periodic regime is found for $Ra_L = 1.82 \times 10^5$ ($\Delta T = 79$ °C). The time history of the acquired velocity (figure 7) shows a periodic trend with nonlinear effects. This nonlinearity gives a large number of resolved harmonics ($\simeq 20$) in the PSD (figure 8). The fundamental frequency is $f = 0.0166$ Hz and a linear best fit of the decay law of the peaks of the harmonics gives a slope of -4.7. As shown by Bishop *et al.* (1968), the unsteadiness is due to a plume oscillating longitudinally out of phase. The oscillation of the plume has been detected in all the visualizations performed (see e.g. § 5.4). Thus, the instability seems to be of a three-dimensional type, according to Bishop *et al.* (1968), Kuehn & Goldstein (1976) and Miki *et al.* (1988).

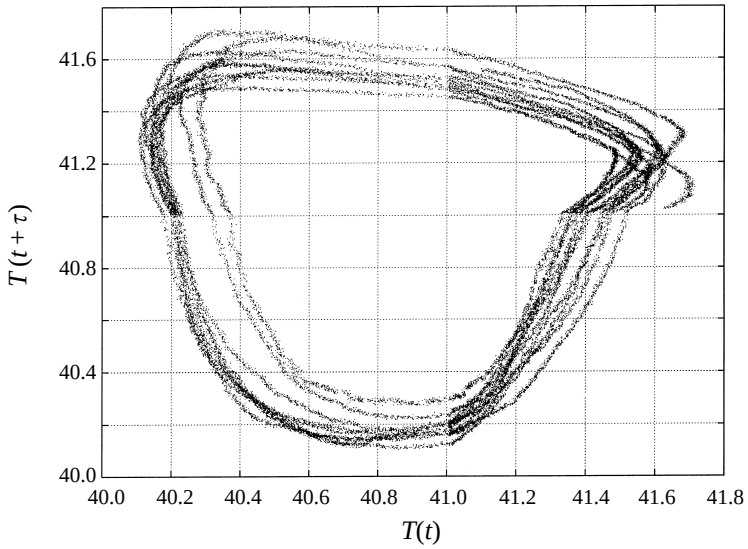

FIGURE 9. Phase trajectories for $Ra_L = 1.82 \times 10^5$. Temperature.

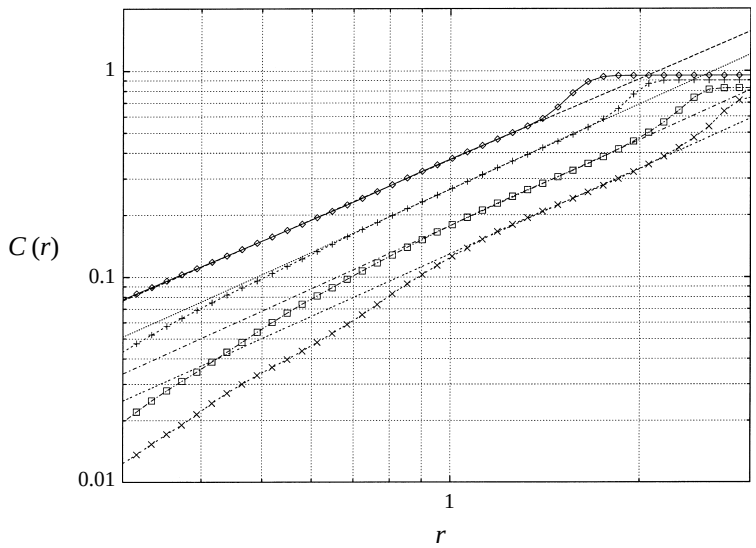

FIGURE 10. Correlation function for $Ra_L = 1.82 \times 10^5$ as a function of the non-dimensional distance r on a log–log scale. The dimension of the phase pseudo-space (n) is the parameter increasing downward. The slope of the power law gives an estimation of the fractal dimension FD $= 1.12 \pm 0.15$.

The PT (figure 9) shows a curve homeomorph to a circle of order 3 with three zones where the density of the points seems greater than the average one which is a cloud of points whose distance is correlated to experimental uncertainty.

The FD is, as described in § 4.3, the slope of the scaling law of $C(r)$ in the linear range not affected by noise (figure 10). All the degrees of freedom considered give an FD of 1.12 ± 0.15. The value is larger than one due to the effect of the large number of harmonics and of noise.

The LE is equal to 0.011 ± 0.012, that is zero within the experimental uncertainty.

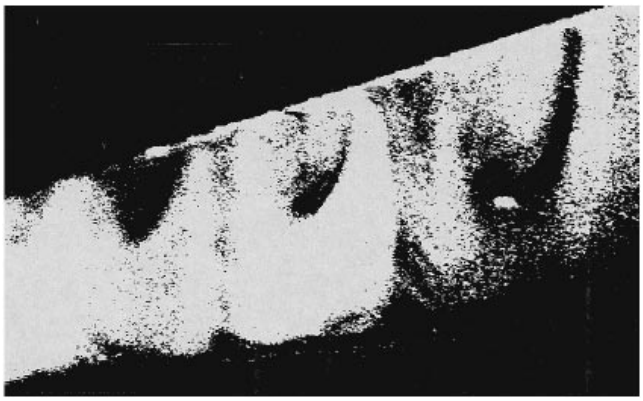

FIGURE 11. Kinematical flow visualization for $Ra_L = 2.15 \times 10^5$ ($\Delta T = 94$ °C) along the axis of the annulus (perspective view).

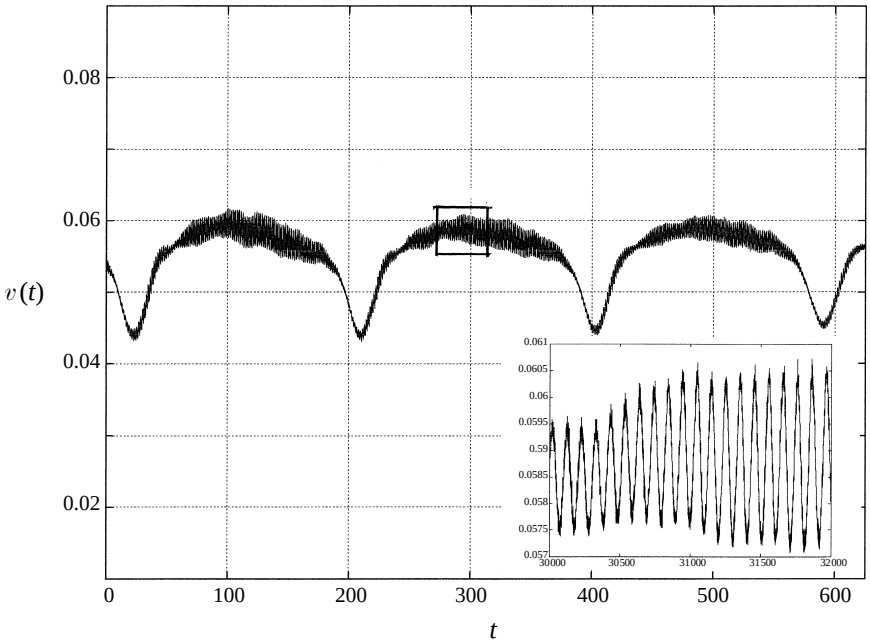

FIGURE 12. The velocity time history for $Ra_L = 2.13 \times 10^5$.

All the considered indicators confirm a monoperiodic behaviour with significant nonlinearity.

5.3. *First quasi-periodic regime*

A quasi-periodic regime is found at $Ra_L = 2.13 \times 10^5$ ($\Delta T = 92$ °C). Flow visualization in the upper region (figure 11) along the axis of the annulus shows a large number of unsteady cross-rolls. The time history of velocity (figure 12) shows regular behaviour with a plateau where the high-frequency oscillations dominate; these plateaus are separated by peaks of stronger intensity at low frequency. Note that the behaviour shown in figure 12 is very similar to that exhibited in figures 13(*c*) and 14(*a*) in Rubio

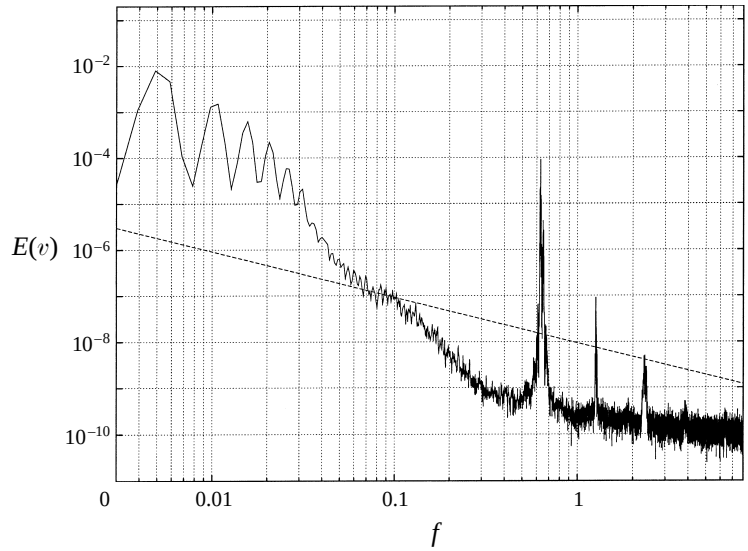

FIGURE 13. Power spectral density for $Ra_L = 2.13 \times 10^5$. Velocity.

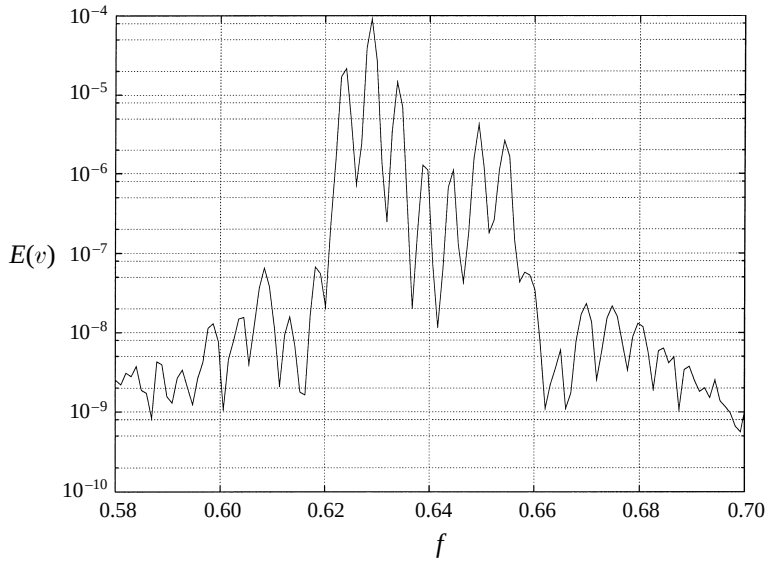

FIGURE 14. Blow up of the power spectral density for $Ra_L = 2.13 \times 10^5$. Velocity.

et al. (1989). This condition corresponds to the maximum negative skewness found, in both temperature and velocity, in the experiments considered. The PSD (figure 13) confirms the presence of two incommensurable frequencies, with a frequency ratio of 128.8 ± 0.1. The low frequency ($f_1 = 0.0049$ Hz), the most energetic, is about 1/3 of that at $Ra_L = 1.82 \times 10^5$. About six harmonics can be detected. In the high-frequency range of the spectrum the highest frequency ($f_2 = 0.628922$ Hz) is detected with two harmonics. By blowing up figure 13 (figure 14) a number of linear combinations $f_2 \pm nf_1$ between the fundamental frequencies are clearly differentiated (Bergé *et al.* 1984).

The PT (figure 15) has the form of a torus with three zones where the density of

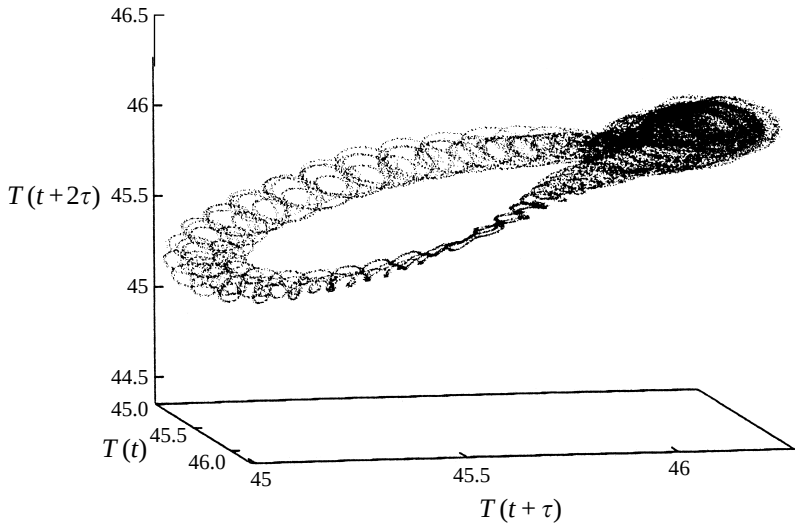

FIGURE 15. Phase trajectories for $Ra_L = 2.13 \times 10^5$. Temperature.

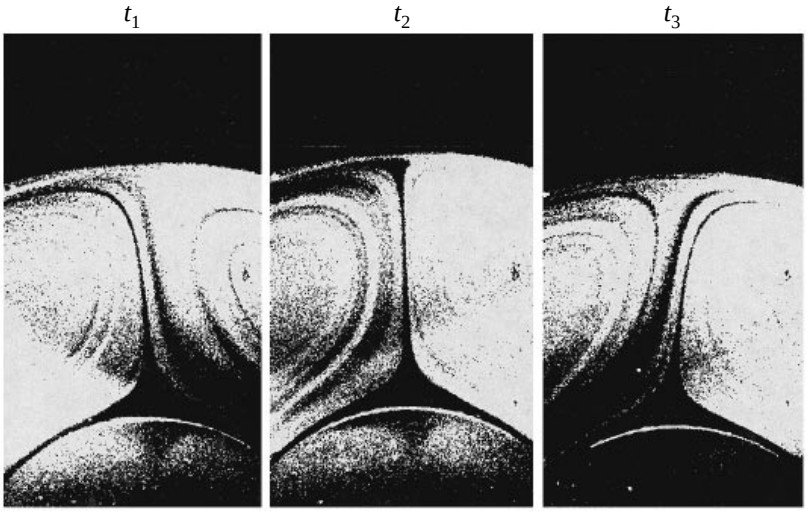

FIGURE 16. Kinematic flow visualization for $Ra_L = 2.45 \times 10^5$ ($\Delta T = 106$ °C) in the upper portion of the transversal mid-plane of the annulus.

points seems greater than the average. The FD is equal to 1.89 ± 0.12 and LE to 0.012 ± 0.012, which confirms the results of the PS.

5.4. *Second periodic regime at high frequency*

By increasing Ra_L to 2.36×10^5 ($\Delta T = 102$ °C) a new periodic regime with $f = 0.665054$ Hz is found. Flow visualization along the axis of the annulus shows quasi-steady cross-rolls of the type of those in figure 11, whereas the transverse visualization shows an oscillating plume (figure 16). The time signal (not presented) is a sinusoid, as confirmed by the PSD (figure 17) where it is evident that the main peak is about 3 orders of magnitude greater than the second and other harmonics. What is interesting

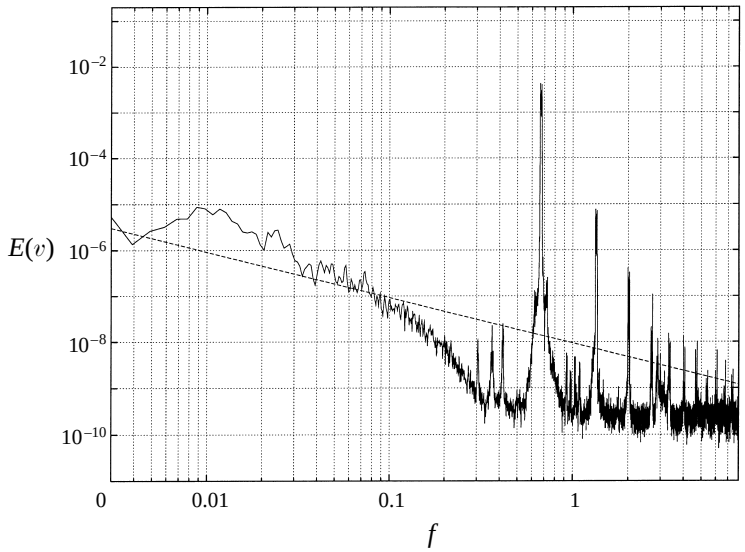

FIGURE 17. Power spectral density for $Ra_L = 2.36 \times 10^5$. Velocity.

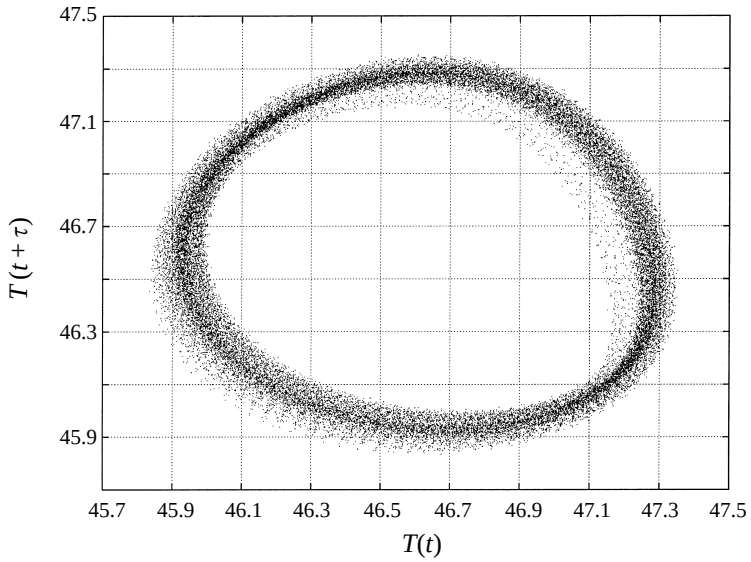

FIGURE 18. Phase trajectories for $Ra_L = 2.36 \times 10^5$. Temperature.

is that the main frequency is only 5.4% greater than f_2 for $Ra_L = 2.13 \times 10^5$, but its energy is two orders of magnitude greater, while the mode at the lower frequency f_1 of figure 13 has largely reduced its energy and seems to disappear.

The fully periodic regime is confirmed also by all the other indicators: the PT is a circle (figure 18), the PS is a point (not presented here), the PDF shows two symmetric peaks (figure 19), the FD is equal to 1.06 ± 0.006 and the LE is equal to 0.005 ± 0.009. With reference to the disappearance of the low frequency f_1, we can guess that the strong energy at a scale which is of the order of the Kolmogorov scale renders the whole system more dissipative and probably stabilizes the large-scale three-dimensional modes.

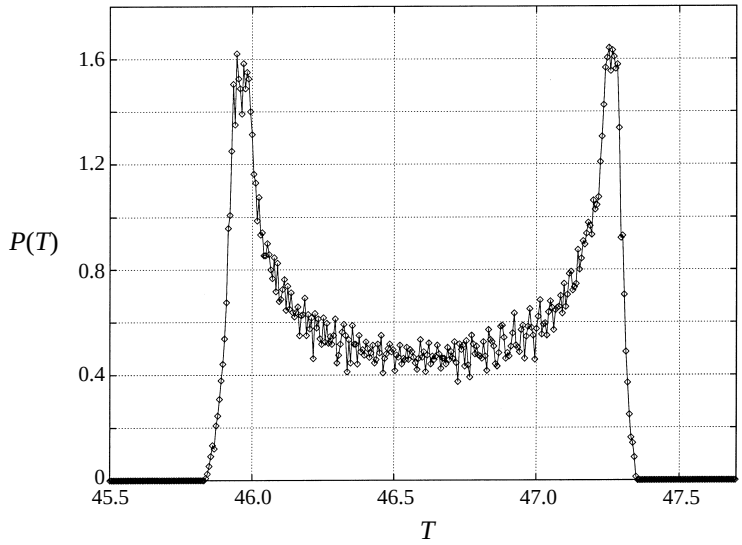

FIGURE 19. Probability density function for $Ra_L = 2.36 \times 10^5$. Temperature.

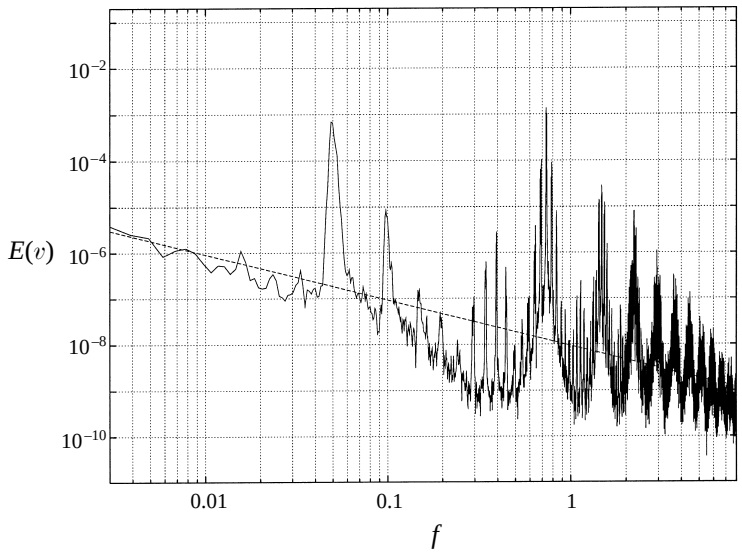

FIGURE 20. Power spectral density for $Ra_L = 2.84 \times 10^5$. Velocity.

This dynamical behaviour is self-maintaining up to $Ra_L = 2.66 \times 10^5$ ($\Delta T = 115$ °C).

5.5. *Second quasi-periodic regime*

A new quasi-periodic regime is found for $Ra_L = 2.84 \times 10^5$ ($\Delta T = 123$ °C). The visualized cross-rolls are still present and unsteady for Ra_L equal to and larger than $Ra_L = 2.84 \times 10^5$. The PSD of the velocity shows (figure 20) that two incommensurable frequencies with the same level of energy are present. The frequency ratio is 15.06 ± 0.01. The fact that the ratio between the two frequencies is irrational is evident from the PT which shows a torus instead of a few points. A large number of harmonics and nonlinear interactions between $f_1 = 0.048830$ Hz and $f_2 = 0.735367$ Hz =

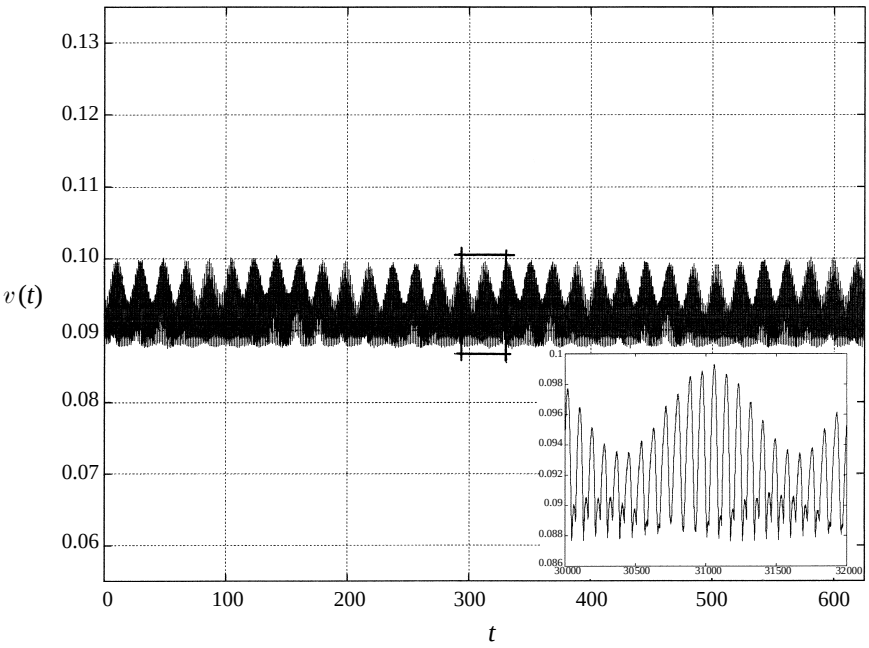

FIGURE 21. The velocity time history for $Ra_L = 2.84 \times 10^5$.

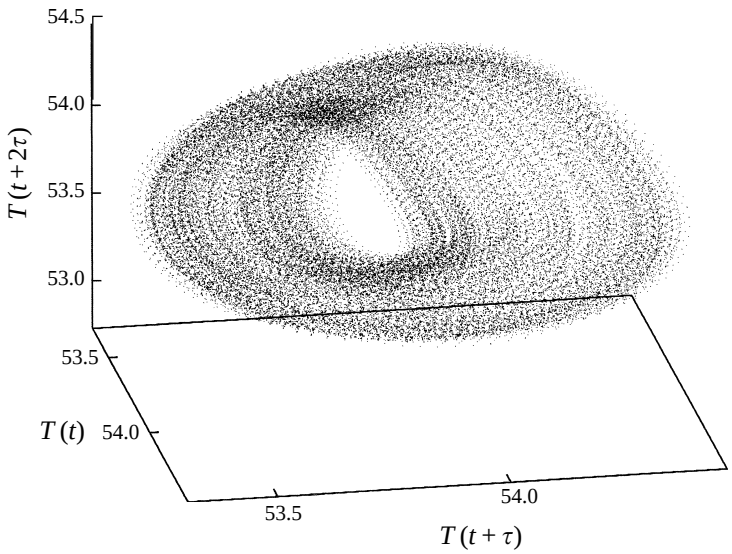

FIGURE 22. Phase trajectories for $Ra_L = 2.84 \times 10^5$. Temperature.

$(15.06 \pm 0.01)f_1$ are clearly detectable on the spectrum. A third small-amplitude frequency is present for $f_3 = 0.394543$ Hz $= (8.08 \pm 0.01)f_1$ with some nonlinear interactions. But, due to the low level of energy, this mode does not affect the quasi-periodic behaviour. The time signal (figure 21) differs significantly from that of figure 12 due to the same level of energy associated to the two frequencies f_1 and f_2.

The PT (figure 22) has the clear form of a torus with a thickness of the same order of magnitude as the diameter. Thus the corresponding PS is, as expected, an ellipse

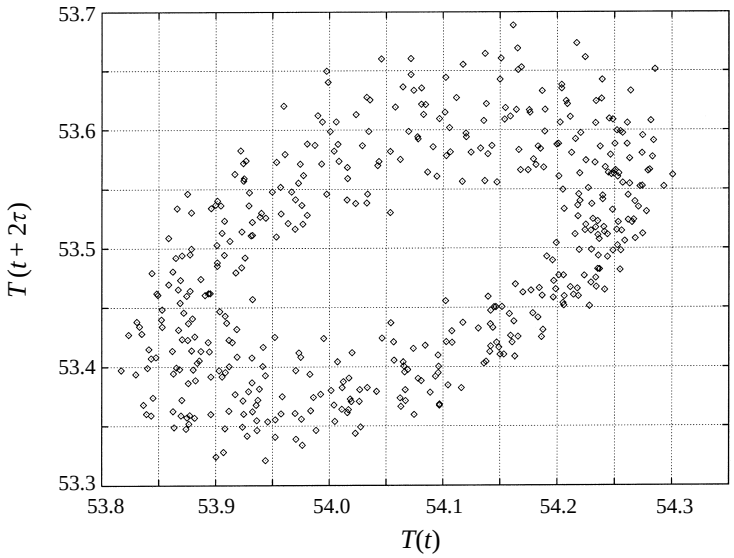

FIGURE 23. Poincaré section for $Ra_L = 2.84 \times 10^5$. Temperature.

(figure 23). The FD is equal to 2.11 ± 0.06 and LE 0.009 ± 0.010. Therefore all the considered indicators confirm the bi-periodic regime.

At $Ra_L = 3.07 \times 10^5$ ($\Delta T = 133$ °C) the behaviour is similar (FD= 2.08 ± 0.06) to that at $Ra_L = 2.84 \times 10^5$, the only difference in the PSD being a slight spreading around the low-frequency ($f_1 = 0.0458998$ Hz) peak and a reduction in the number of harmonics of f_2 ($f_2 = 0.772476$ Hz $= (16.83 \pm 0.01) f_1$). The energy of the third frequency at $f_3 = 0.408216$ Hz $= (8.89 \pm 0.01) f_1$ increases by about one order of magnitude; but the effect is still negligible. Note that for $Ra_L = 3.07 \times 10^5$ the incommensurable nature of the three frequencies is more evident than for $Ra_L = 2.84 \times 10^5$.

5.6. *Chaotic regime*

A small increase in Ra_L up to $Ra_L = 3.37 \times 10^5$ ($\Delta T = 146$ °C) produces a large change in the dynamics of the system, which shows a chaotic behaviour as confirmed by FD $= 5.38 \pm 0.02$ (figure 24) and LE $= 0.30 \pm 0.014$. The time signal is shown in figure 25 and the corresponding PSD, reported in figure 26, exhibit the three frequencies already detected, $f_1 = 0.0449232$ Hz, $f_2 = 0.788101$ Hz $= (17.5 \pm 0.01) f_1$ and $f_3 = 0.417005$ Hz $= (9.08 \pm 0.01) f_1$, few harmonics or nonlinear interactions and a wide spreading at high frequencies. At low frequency, the spectrum presents a turbulent trend with a low-frequency energy-containing range and a range presenting a scaling law, which seems to be dissipative (exponent -6.56).

The chaotic regime is confirmed by the PT (figure 27) and the PS (not shown) with the dispersion of the points in shape of a cloud. The PDF (figure 28) gives an exponential trend which seems to show the presence of intermittent behaviour (Heslot, Castaing & Libchaber 1987).

Finally, in order to compare the temperature variations for various Ra_L, in figure 29 all the PTs are reported on the same scale.

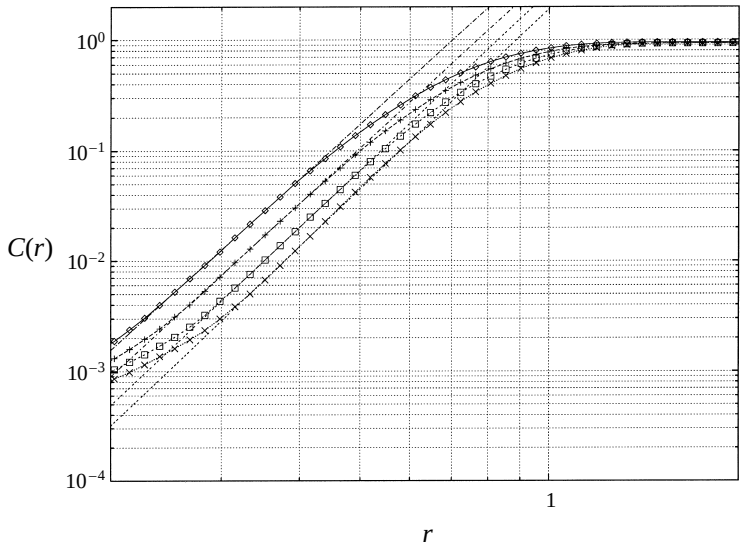

FIGURE 24. Correlation function for $Ra_L = 3.37 \times 10^5$ as a function of the non-dimensional distance r on a log–log scale. The dimension of the phase pseudo-space (n) is the parameter increasing downward. The slope of the power law gives an estimation of the fractal dimension FD $= 5.38 \pm 0.02$.

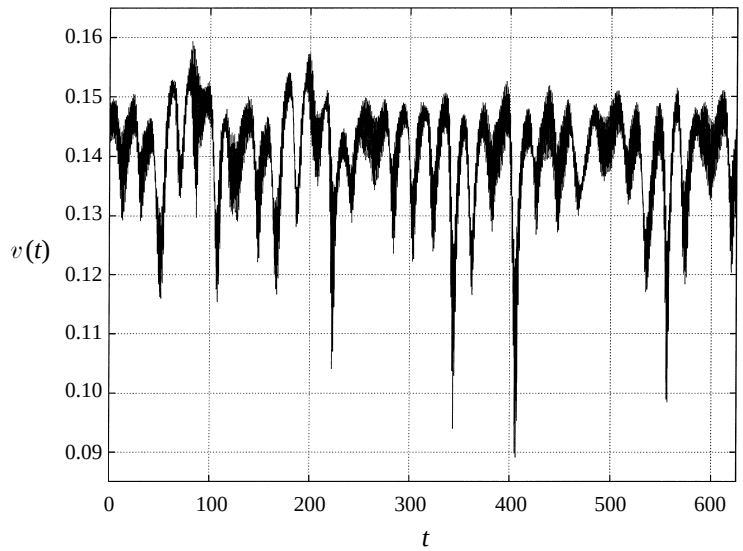

FIGURE 25. The velocity time history for $Ra_L = 3.37 \times 10^5$.

6. Conclusions

A study of natural convection in a cylindrical annulus has been conducted in a range of Ra_L ($0.9 \times 10^5 < Ra_L < 3.37 \times 10^5$), which is characteristic of gas-insulated electric transmission cables. Also the considered non-dimensional gap ℓ ($\ell = 0.68$) is a standard value for many engineering applications such as long-distance transmission cables and power substations.

By systematic experimental analysis it has been verified that the mechanism of

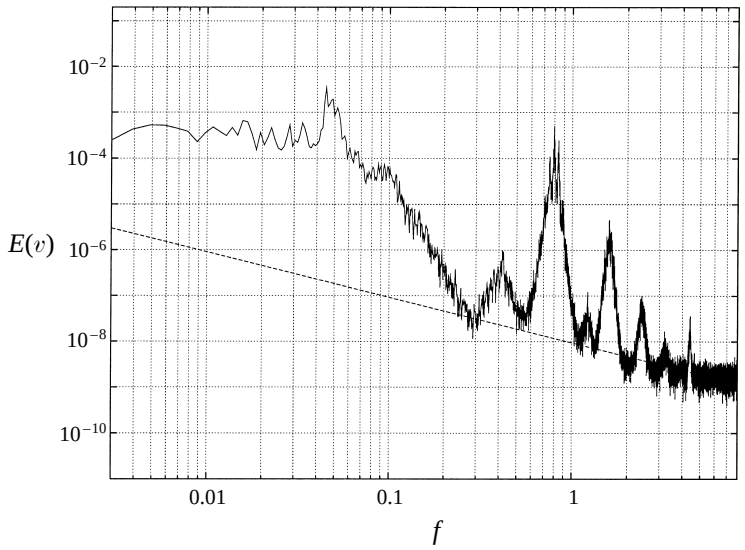

FIGURE 26. Power spectral density for $Ra_L = 3.37 \times 10^5$. Velocity.

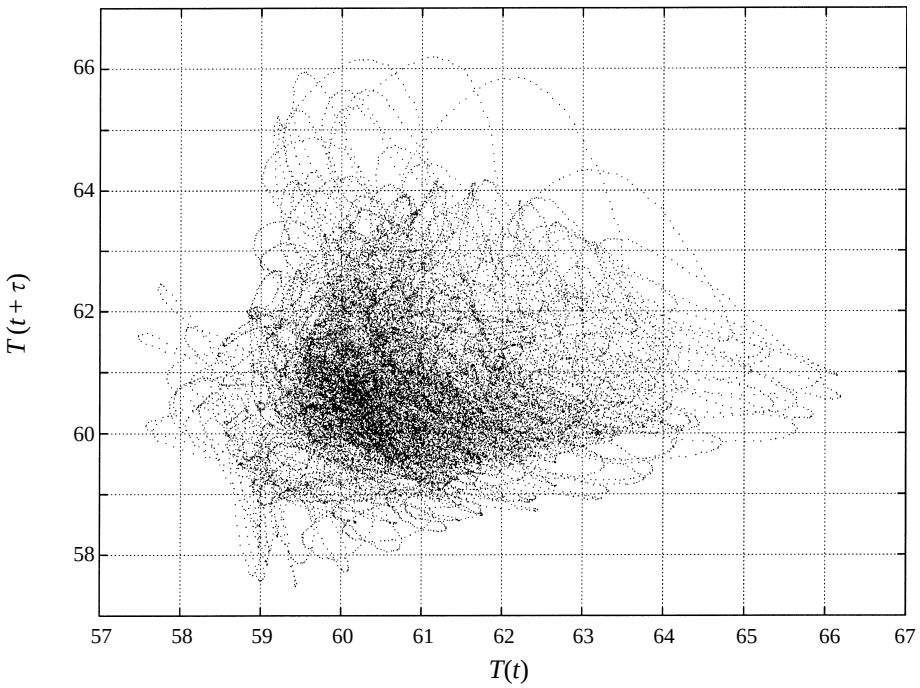

FIGURE 27. Phase trajectories for $Ra_L = 3.37 \times 10^5$. Temperature.

transition from steady state to chaotic turbulent conditions is quite repeatable and the following stages in the transition to chaos have been differentiated by different dynamical indicators: 2D steady state; first periodic regime at low frequency with an oscillating flow of 3D type; first quasi-periodic regime for the growth of a high-frequency mode due to a large number of unsteady cross-rolls; second periodic regime at high frequency with quasi-steady cross-rolls and transverse oscillation of

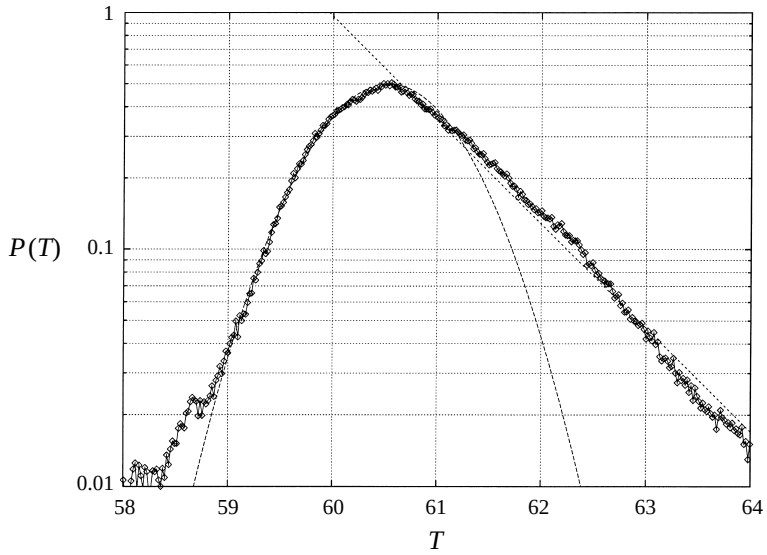

FIGURE 28. Probability density function for $Ra_L = 3.37 \times 10^5$. Temperature.

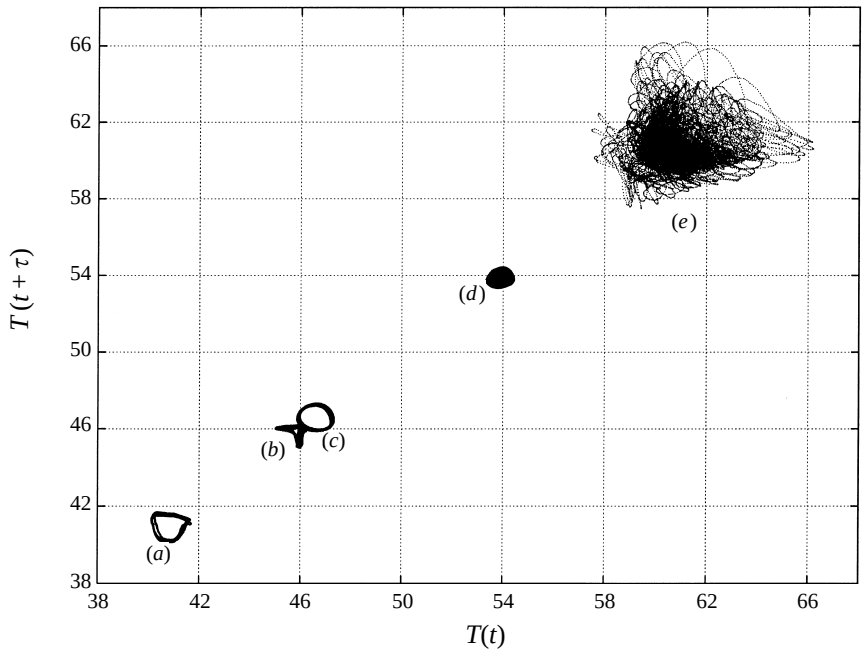

FIGURE 29. Phase trajectories for: (*a*) $Ra_L = 1.82 \times 10^5$; (*b*) $Ra_L = 2.13 \times 10^5$; (*c*) $Ra_L = 2.36 \times 10^5$; (*d*) $Ra_L = 2.84 \times 10^5$ and (*e*) $Ra_L = 3.37 \times 10^5$. Temperature.

the plume; second quasi-periodic regime and finally transition to chaos. The final stage of transition to chaos follows a route which seems to fit the Curry–Yorke scenario because the third incommensurable frequency presents an energy level negligible with respect to the other two.

This well defined route to chaos is, on the other hand, not expected for smaller gaps which can present multicellular solutions of Rayleigh–Bénard type in

the upper part of the annulus. So in geometries with very small gaps different mechanisms of transition to chaos can be found depending on the initial conditions and noise.

The repeatability and robustness of the mechanism of transition to chaos of the considered annulus in connection to the increasing capability for heat exchange in chaotic (turbulent) unsteady conditions with respect to steady laminar ones (larger Nusselt number v/s Ra_L slope) seems to confirm that the adopted gap corresponds to a stable system from the global thermal point of view.

Professor M. Behnia is acknowledged for his helpful comments. The authors would also like to thank Drs F. Stella, R. Camussi and P. Capoferro for their collaboration in setting up the experiment and the measurement technique.

REFERENCES

Atten, P. & Malraison, B. 1988 Caractérisation du chaos déterministe rencontre dans les expériences. *Le Chaos* (*Collection CEA*), pp. 283–325.

Baker, G. L. & Gollub, J. P. 1990 *Chaotic Dynamics: an Introduction.* Cambridge University Press.

Benettin, G., Galgani, L. & Strelcyn, J. M. 1976 *Phys. Rev.* A **14**, 2338.

Bergé, P., Pomeau, Y. & Vidal, C. 1984 *Order within Chaos.* John Wiley & Sons.

Bishop, E. H., Carley, C. T. & Powe, R. E. 1968 Natural convective oscillatory flow in cylindrical annuli. *Intl J. Heat Mass Transfer* **11**, 1741–1752.

Brunn, H. H. 1995 *Hot-Wire Anemometry: Principles and Signal Analysis.* Oxford University Press.

Carlomagno, G. M. 1986 Metodi ottici quantitativi nella diffusione di massa e di energia. *UIT Atti del* 4° *Congresso Nazionale Sulla Trasmissione del Calore, June 5–7, Genova, Italy.*

Chakrabarti, S., Probert, S. D. & Shilton, M. J. 1983 Optimal eccentrical annuli (containing atmospheric-pressure air) for thermally insulating, horizontal, relatively cold pipes. *Appl. Energy* **14**, 257–293.

Cho, C. H., Chang, K. S. & Park, K. 1982 Numerical simulation of natural convection in concentric and eccentric horizontal cylindrical annuli. *J. Heat Transfer* **104**, 624–630.

Farmer, J. D., Ott, E. & Yorke, J. A. 1983 The dimension of chaotic attractors. *Physica* D **7**, 153–180.

Grassenberger, P. & Procaccia, I. 1983 Characterization of strange attractors. *Phys. Rev. Lett.* **50**, 346–349.

Guj, G., Iannetta, S. & Moretti, G. 1992 Experimental analysis of thermal fields in horizontally eccentric cylindrical annuli. *Exps. Fluids* **12**, 385–393.

Guj, G. & Stella, F. 1995 Natural convection in horizontal eccentric annuli: numerical study. *Numer. Heat Transfer* **27** (A), 89–105.

Guj, G., Labonia, G. & Stella, F. 1997 Digital procedure for simultaneous velocity and temperature measurements by hot/cold wire anemometers. *Proc. Eurotherm Seminar 55, Santorini, Greece.*

Heslot, F., Castaing, B. & Libchaber, A. 1987 Transitions to turbulence in helium gas. *Phys. Rev.* **36**, 5870–5873.

Kuehn, T. H. & Goldstein, R. J. 1976 An experimental and theoretical study of natural convection between horizontal concentric cylinders. *J. Fluid Mech.* **74**, 695–719.

Kuehn, T. H. & Goldstein, R. J. 1978 An experimental and theoretical study of natural convection heat transfer in concentric and eccentric horizontal cylindrical annuli. *J. Heat Transfer* **100**, 635–640.

Merzkirch, W. 1974 *Flow Visualization*, pp. 115–231. Academic.

Miki, Y., Ohya, T., Morita, K., Fukuda, K. & Hasegawa, S. 1988 Unsteady three-dimensional behaviour of natural convection in horizontal annulus, (II) Flow patterns in range from transition region to turbulence and measurements of turbulence quantities. *J. Atomic Energy Soc. Japan* **30** (2), 172–180.

Ohya, T., Miki, Y., Morita, K., Fukuda, K. & Hasegawa, S. 1989 Unsteady three-dimensional behaviour of natural convection in horizontal annulus. *J. Atomic Energy Soc. Japan* **30** (1), 87–96.

Oseledec, V. I. 1968 *Trudy Mosk. Mat. Obsc.*, **19** 179 (*Moskow Math. Soc.* **19**, p. 197).

Prusa, J. & Yao, L. S. 1983 Natural convection heat transfer between eccentric horizontal cylinders. *J. Heat Transfer* **105**, 108–116.

Rubio, M. A., Bigazzi, P., Albavetti, L. & Ciliberto, S. 1989 Spatio-temporal regimes in Rayleigh–Benard convection in a small rectangular cell. *J. Fluid Mech.* **209**, 309–324.

Takens, F. 1981 *Detecting Strange Attractors in Turbulence*. Lecture Notes in Mathematics, vol. 898, pp. 366–381. Springer.

Wang, Y. Z. & Bau, H. H. 1988 Low Rayleigh number convection in horizontal eccentric annuli. *Phys. Fluids* **31**, 2467–2473.